A COMPARISON OF NUMERICAL RANS SIMULATIONS AND FLOW FIELD MEASUREMENTS OF AN OSCILLATING AIRFOIL FOR FLAPPING WING PROPULSION

Stephan Bansmer*, Ekrem Mazlum*, Rolf Radespiel*
*** Institute of Fluid Mechanics, Bienroder Weg 3, 38106 Braunschweig, Germany**

Abstract

The flow at Reynolds number 100k around an inflexible, two-dimensional flapping airfoil is investigated using the stereoscopic Particle Image Velocimetry (PIV) technique. The typical phenomenon of a moving laminar separation bubble during one flapping cycle is identified. The measurement data is compared with URANS computations.

1 Introduction

The outstanding flight performance of birds raises the question whether the flapping flight mechanism is advantageous compared to propeller generated thrust in the low Reynolds number range. To answer this question, the balance between drag and thrust has to be evaluated, focusing on the determination of the propulsive efficiency. Considering that there is a great variety of possible kinematical flapping configurations, this task can only be accomplished through numerical simulations.

Dealing with unsteady numerical simulations in the low Reynolds number range includes many challenges:

- to choose the appropriate turbulence model
- to handle the phenomenon of the laminar separation bubble (LSB)
- to predict the transition from laminar to turbulent flow within separated flows

Nevertheless, RADESPIEL et al. demonstrated the capability of numerical flow simulations in this area by investigating the flow around a flapping SD7003 airfoil [1] using simple heaving motion. In the present contribution, a new, birdlike airfoil, named SG04 [2], is investigated, see fig. 1. Its shape is based on the hand pinion of a seagull.

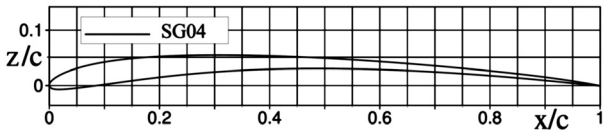

Figure 1: The birdlike airfoil SG04

The numerical flow simulation (URANS solver) of the new SG04 airfoil is compared with PIV data of new kinematic flapping case. The paper is divided into four main sections:

- Introduction into the aerodynamics of moving airfoils
- Numerical simulation scheme
- Experimental setup
- Comparison between numerical URANS simulations and experimental data

2 Aerodynamics of moving airfoils

In our case, the two-dimensional flapping case is discussed, i.e. three-dimensional effects in boundary layer flow and trailing vortices are neglected.

As shown in fig. 2, the flapping motion is composed of a heaving and a pitching motion which can be described by the equations:

$$z(t) = \hat{z} \cdot \cos(\omega t)$$
$$\varphi(t) = \hat{\varphi} \cdot \cos\left(\omega t + \pi/2\right) + \varphi_0 \qquad (1)$$

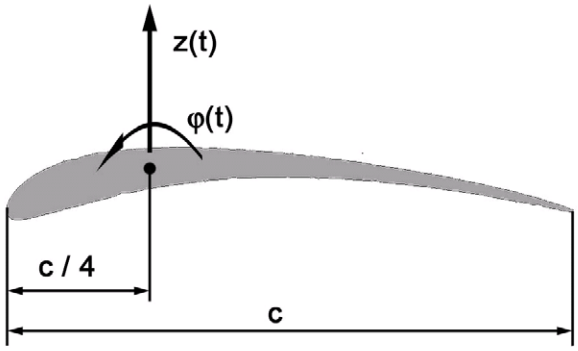

Figure 2: The airfoil motion

An oscillating sliding motion in the direction of the oncoming flow is not considered.

Due to the heaving motion, the geometrical angle of attack $\varphi(t)$ is distorted into an effective angle of attack $\alpha_{eff}(t)$, see fig. 3. If the airfoil moves downwards – in negative z-direction -, the airfoil will experience this distortion in its frame of reference as if the oncoming wind would create a much larger angle of attack.

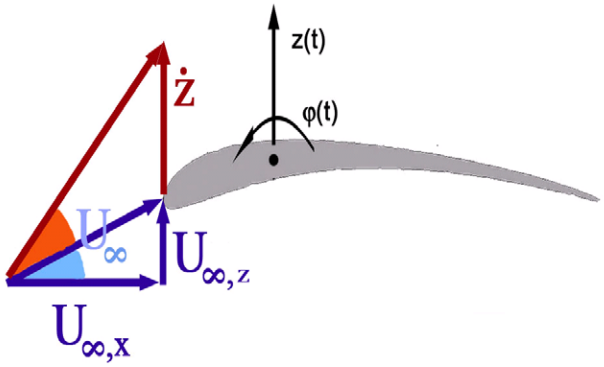

Figure 3: Distortion of the geometrical angle of attack during the flapping motion

This distortion $\zeta(t)$ of the geometrical angle of attack can be described by the equation:

$$\zeta(t) = \arctan\left[-\frac{\dot{z}(t)}{U_\infty}\right] \qquad (2)$$

Hence, the effective angle of attack yields:

$$\begin{aligned}\alpha_{eff}(t) &= \varphi(t) + \zeta(t) \\ &\approx \Delta\alpha_{eff} \cdot \sin(\omega t) + \varphi_0\end{aligned} \qquad (3)$$

Note that the pitching motion also creates additional induced velocities which are varying along the airfoil surface. These velocity components are neglected in the concept of the effective angle of attack, but they can be considered as a change in the camber of the airfoil.

Regarding the kinematics of flapping flight, many parameter studies had been carried out in the past both experimentally [16,17,18] and numerically [19,20,21]. Many of those studies consisted of changing only one kinematical parameter as for example flapping frequency, heaving or pitching amplitude, et cetera. For selecting the kinematical parameters in the present contribution, multiple parameters were changed simultaneously according to the suggestions by the inviscid flapping flight theory of KÜSSNER [22], see also [15]. The result was a configuration with a high propulsive efficiency at a moderate flapping frequency.

In this article, one kinematical flapping case is discussed in detail. Its parameter set is given by:

- $\mathrm{Re} = 10^5 \longrightarrow U_\infty \approx 8\,\frac{m}{s}$
- chord length $c = 0.2m$
- $k = \pi \cdot f \cdot c / U_\infty = 0.2$
- $\hat{z} = 0.1m$
- $\varphi_0 = 4°$
- $\Delta\alpha_{eff} = 4° \longrightarrow \hat{\varphi} = 7.46°$

Besides these geometrical considerations, there is also an interesting aerodynamic phenomenon occurring in this Reynolds number range: the laminar separation bubble (LSB) [13,14], see fig. 4.

Depending on the Reynolds number, the flow around the airfoil is considered with conventional numerical methods either laminar or turbulent. However, at the investigated Reynolds number of 100k, the flapping airfoil shows transitional behavior which is fully covered by the present numerical code [15]. This is of great importance since the laminar separation bubble is moving along the airfoil surface during one flapping cycle. It has in

consequence a reasonable influence on the airfoil drag as well as on the propulsive efficiency.

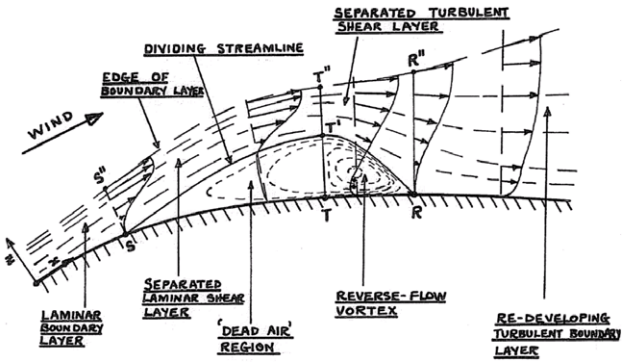

Figure 4: The laminar separation bubble [3]

The physics of the LSB can be described as follows. The oncoming laminar flow separates, which is caused by a pressure elevation along the airfoil contour. From SPALART and STRELETS [4], the separated flow performs the transition process from laminar to turbulent flow due to Kelvin-Helmholtz instabilities [5]. Thus, the turbulent fluctuations in the flow enhance momentum transport towards the wall, and the flow reattaches to the airfoil contour. The enfolded region of circulating flow is called the LSB. LSB's are usually not desired in airfoil design because they elevate the pressure drag of the airfoil due to an increased displacement thickness level of the boundary layer. Hence, the original design approach of the SG04 airfoil was to minimize the size of LSB as much as possible [2].

3 Numerical Algorithm

The numerical algorithm is based on the work of RADESPIEL et al. [1] and WINDTE et al. [7]. In this chapter, the main features are briefly highlighted. The objective is to determine accurate engineering solutions for the flow around a flapping airfoil in the ensemble-averaged mean, along the motion.

An unsteady Reynolds-averaged Navier-Stokes (URANS) solver, called FLOWer [8] is used to simulate low Reynolds number flows. The solver requires block-structured meshes; its discretization algorithm uses a finite volume approach. A second-order accurate central difference algorithm with scalar dissipation was applied to evaluate convective fluxes. Implicit residual smoothing, local time stepping, low-speed preconditioning and multigrid operations were performed to accelerate the computation. A second-order accurate implicit dual time stepping algorithm was used for the time-accurate computations. The Menter-Baseline model [9] was chosen for turbulence modeling. Its equations were computed separately on a single grid basis.

The most important challenge is to model the physics of the LSB. The transition process around the LSB is executed in three steps. In the *first stage*, small harmonic disturbances are generated through external distortions. This receptivity mechanism can not be modeled by the RANS equations. In the *second stage* of the transition process, some of the unstable harmonic waves grow exponentially while traveling downstream. This behavior can be described very well by the linear stability theory. In Ref. [8] a new formulation of the stability problem is used that takes into account the effects of unsteady boundary layer mean flow on the travelling waves. The linear stability analysis is done using the solver LILO [10] which assumes the boundary layer as a parallel flow. The harmonic wave assumption is applied to the variables velocity, pressure and temperature in the boundary layer. Then a set of five linear differential equations – the temporal stability problem - is solved by determining the eigenvalues of the problem. The transition process is completed in the *third stage*. There, the distortions become so large, that secondary instabilities can grow in the boundary layer connected with strong nonlinear interactions in the flow. These nonlinear interactions finally yield to a breakdown in the laminar flow structure. This stage is not directly integrated into the numerical code since it passes very rapidly. The distance between the locations of the end of the second and third transition stage is very small. However, the spatial extent of the third stage can be simulated by choosing an appropriate higher critical N-factor, so the linear amplification of the harmonic waves is

extrapolated. The turbulence transport equations are activated at the point of the predicted transition.

The result of the numerical simulations is a mean flow field $\langle \vec{v} \rangle$ for every phase during one flapping cycle. Furthermore, the determination of the *turbulent shear stress* is of great significance. Its quantity is an indicator for the turbulent momentum transport across the boundary layer. Hence, it displays the beginning of the closure of the LSB. From the URANS computations, it can be recovered using the BOUSSINESQ approximation, which is given by:

$$\tau_{xy} = -\rho \cdot \overline{u'v'} = \mu_t \cdot \left(\frac{\partial \langle u \rangle}{\partial y} + \frac{\partial \langle v \rangle}{\partial x} \right) - \left(\overline{u \cdot v} - \bar{u} \cdot \bar{v} \right) \quad (4)$$

Herein, $\langle u \rangle$ and $\langle v \rangle$ denote the ensemble average of the velocity components u and v. The second part of this equation takes mean flow oscillations into account as they sometimes occur during numerical simulations when vortices are shed downstream from the LSB [7]. For thin LSBs, which are considered in the present computation, the second part of the equations is usually close to zero and it is not accounted in the present results.

4 The measurement and its data evaluation

The objective of the measurements is to capture the flow and its turbulent quantities in the boundary layer of the flapping airfoil with the given kinematical scheme at four different phase angles.

Therefore, the experiments were carried out on the Low Speed Low Noise Wind Tunnel (LNB), see fig. 5. The inlet is composed of a fleece mat of 30 millimeter (1.18 in.) in thickness. Afterwards, the air passes a straightener made out of aluminum honeycombs, 14 millimeter (0.55 in.) in diameter, 200 millimeter (7.87 in.) in length and a fine-mesh woven screen. In the large settling chamber, small scale turbulence is dissipated, and a Boerger-type nozzle contracts the air to a 16:1 ratio. Consequently, the air has a turbulence level of better than 0.1 percent in the 400 x 600 millimeter (15.75 x 23.62 in.) sized test section. The wind tunnel is driven by a 4 kW (5.2 hp), acoustically encapsulated, speed-controlled three-phase asynchronous motor, which produces a flow speed in the test section from 5 up to 20 meters per second (11.2 to 44.7 mph). The laboratory is lined with open-celled acoustic foam [11].

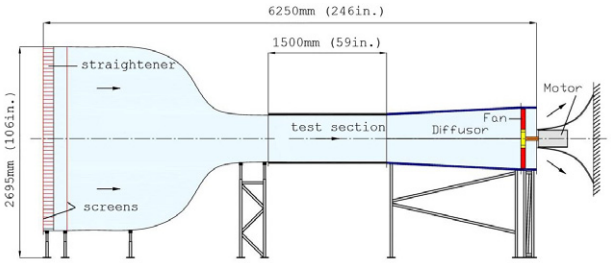

Figure 5: The wind tunnel LNB

The moving airfoil motion apparatus is mounted around the test section. Its primary task is to create the heaving and the pitching motion of the airfoil corresponding to the equations (1) and the parameter set given in chapter 2.

The velocity field of the boundary layer is measured with the stereoscopic particle image velocimetry technique; see the top view on the wind tunnel in fig. 6. For this, a laser light sheet was created normal to the airfoil surface at the half wing span. Two PCO 4000 cameras capture the particle images with a window size of 60 x 25 millimeters. This is necessary to resolve the flow in the boundary layer. However, the window size is very small compared to the overall dimensions of the flapping motion, as depicted in fig. 7. Therefore, the camera system had to be mounted on a translation device in order to move the system in heaving and chord wise direction without changing the alignment of the cameras. The stereoscopic setup was necessary because the motion apparatus avoids direct visible access normal to the laser light sheet. Thus, standard PIV measurements were not possible.

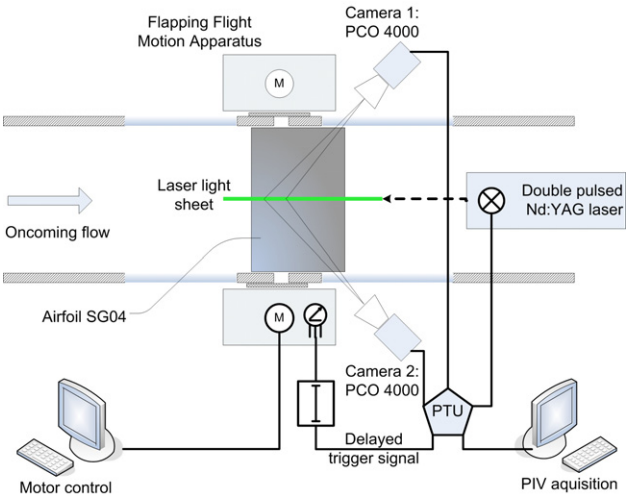

Figure 6: Top view of the PIV setup

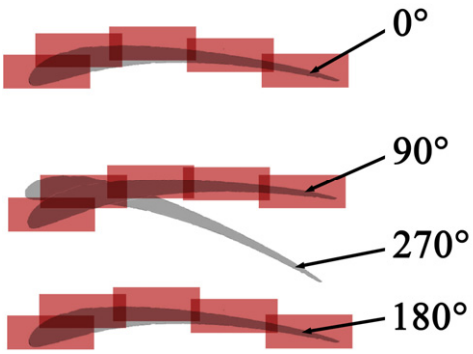

Figure 7: PIV measurement windows to capture one flapping cycle. For clarity reasons, the measurement windows are not depicted at a phase of 270° [12].

To capture the flow field at a constant phase angle, phase locked imaging was performed. For this purpose, a TTL signal from a light barrier from the motion apparatus (which triggers at the beginning of each flapping cycle) was captured and shifted in time by a Stanford delay generator DG 535. When the delayed signal was detected by the Programmable Timing Unit (PTU9 by LaVision), the laser flash and the camera exposure were initiated, see also fig. 6.

Table 1 gives a complete summary of the employed measurement equipment.

Laser data	
Type	Quantel Brilliant double pulsed Nd:YAG
Energy	2 x 150mJ
Wavelength	532nm
Camera system	
Cameras	2 x PCO 4000
Resolution	4008 x 2672 px
Objectives	Tamron f = 180mm
Data Transfer	Firewire
Seeding	
Particles	Oil particles
Particle Diameter	About 1µm
PIV System Triggering	
Camera and Laser Triggering	Programmable Timing Unit (PTU 9) by LaVision
PIV Software	
Software	Davis 7.1 by LaVision for data acquisition and Davis 7.2 for data evaluation

Table 1: PIV measurement equipment

4.1 Data evaluation

Once the particle image acquisition of 500 image pairs for each of the twenty measurement windows was completed, the velocity vector field of the flow around the airfoil and its turbulent quantities had to be determined.

At first, a wobble correction was performed. When the laser light sheet reaches the airfoil surface, the so called reflection line is visible on the camera images. Due to the phase locked imaging, this reflection line which indicates the position of the airfoil should be always at the same location. However, the reflection line is wobbling about 0.5 millimeters in the camera images. This wobbling had to be cleared since the airfoil has to be at the same position for the later ensemble averaging procedure of the vector fields (to compute the mean flow vector field, etc.).

Having completed several image preprocessing techniques to improve the particle image quality, the particle displacement evaluation was executed in the next step using a cross correlation scheme. A multipass interrogation

scheme was applied with decreasing interrogation window size (from 128x128 pixels down to 32 x 32 pixels), 50% overlap and elliptical weighting function.

The resulting set of 500 vector fields for each measurement window was later post processed. This was necessary to filter out non physical vectors in the vector fields which would corrupt the results of the ensemble averaging procedure.

The ensemble averaging is the statistical task to compute among other things the mean velocity field given by the equation:

$$\left\langle \vec{v}\left(\vec{x},t\right)\right\rangle = \frac{1}{n}\sum_{i=1}^{n}\vec{v}_i\left(\vec{x},t\right) \qquad (5)$$

Furthermore, the turbulent shear stress τ_{xy} can be determined by the relation

$$\begin{aligned}\tau_{xy} &= -\rho\cdot\left\langle u'\cdot v'\right\rangle \\ &= -\rho\cdot\frac{1}{n}\sum_{i=1}^{n}\left\{\left[u_i-\left\langle u\right\rangle\right]\cdot\left[v_i-\left\langle v\right\rangle\right]\right\}\end{aligned} \qquad (6)$$

The criterion $\tau_{xy}/\left(\rho\cdot U_\infty\right)=0.1\%$ was used to define the position of transition from the PIV data.

Finally, each of the five measurement windows per investigated phase angle had to be placed at the correct position on the airfoil to obtain the complete distribution along the airfoil surface which corresponds to the computed quantities. This operation was carried out using TECPLOT.

5 Results and comparison

Before the numerical and experimental investigations are compared in detail, some of the most important results of the numerical simulations shall be presented. The critical N-factor used in the simulation was set to 10, in accordance with the turbulence level of 0.1%. The lift coefficient plot over one flapping cycle is depicted in in fig. 8. On the abscissa, the non-dimensional time is printed with a value range from 2 to 3. This therefore represents an intervall out of the full numerical simulation which start at t/T=0. The solution needs about 2 flapping cycles to reach its asymptotic distribution. The upper dead center of motion passes when t/T is an integer. Consequently, the first half of the flapping cycle belongs to the downstroke and the second part to the upstroke. The lift plot itself reveals that the flapping configuration produces lift during the whole cycle. Maximum lift is obtained *shortly after* the middle of the downstroke. Hence, the lift does not peak at the largest effective angle of attack α_{eff} of 8° at t/T=2.25. Rather, there is a delay between maximum lift and maximum effective angle of attack due to *unsteady effects*. This delay is also visible through the smallest lift coefficient, which occurs shortly after the smallest effective angle of attack of 0° at t/T=2.75.

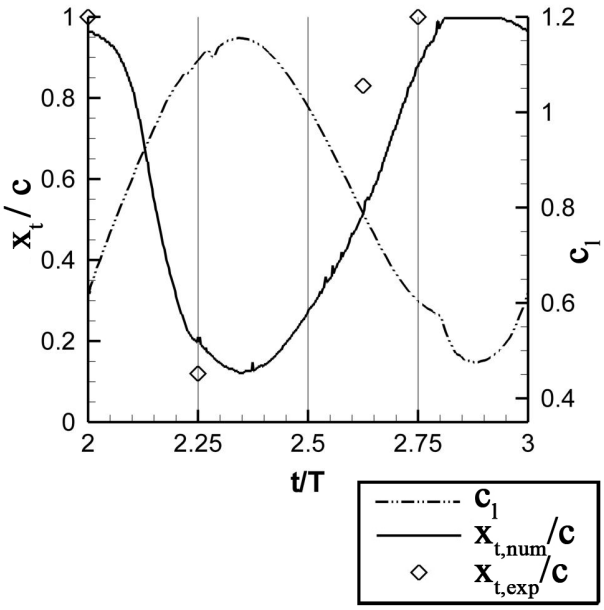

Figure 8: Lift coefficient and transition location over one flapping cycle. Experimental results are marked with a diamond.

Fig. 8 also shows the plot of the transition position during one flapping cycle. As depicted, the transition location moves from the trailing edge to the leading edge during the downstroke. During the upstroke it is vice versa. Note, that the transition movement from the trailing to the leading edge is twice as fast as the movement during the upstroke. It is interesting to consider that the transition movement towards the trailing edge starts when the lift coefficient reached its maximum.

In order to initially compare experimental results, the measured transition location is marked with diamonds on four phase angles. The general behavior of the transition movement is consistent with the numerical prediction. The transition locations at the phase angles 0°, 90° and 270° especially concur with the numerical results. There is a significant discrepancy only at 225° phase angle. Thus, a further measurement at the phase 180° was carried out in order to compare whether at least the gradient $\partial(x_t/c)/\partial(t/T)$ during the upstroke is in agreement with the numerical simulation. However, there are no results available at this time.

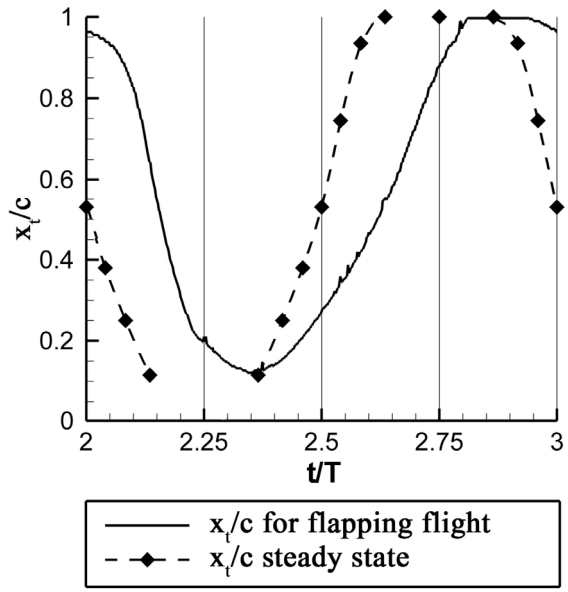

Figure 9: Lift coefficient and transition location over one flapping cycle. Experimental results are marked with a diamond.

Furthermore, the numerical code was employed to simulate the flow under steady conditions at different angles of attack, i.e. the flapping motion set to zero. As discussed in section 2, the flapping motion has at every phase angle an effective angle of attack. This is the angle of attack which the airfoil would see under steady conditions. Hence, it is possible to compare the transition location from laminar to turbulent flow at every phase angle between the unsteady solution of the kinematical flapping case and the corresponding steady state solution at an equal effective angle of attack, see therefore fig. 9. The differences in the two plots are clearly visible. They are a result of the unsteady aerodynamic effects in flapping flight.

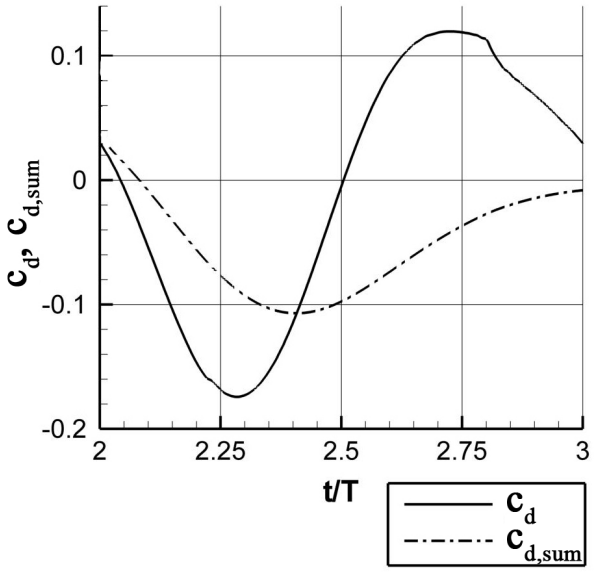

Figure 10: Drag coefficient and net drag coefficient over one flapping cycle.

Another result of the numerical simulations is the distribution of the drag coefficient over one flapping cycle, see fig. 10. Under steady conditions, the drag coefficient of an airfoil will always have a value greater than zero. However, by analyzing fig. 10, the drag coefficient is periodically changing its value and obtains negative amounts that is thrust during the downstroke. To get an idea which how much net thrust is produced per flapping cycle, the thrust coefficient can be integrated over time, given by the equation:

$$\tau \rightarrow \tau = \frac{t}{T}$$
$$c_{d,sum}(\tau) = \frac{1}{\tau - \tau_{start}} \cdot \int_{\tau_{start}=2}^{\tau} c_d \cdot d\tau^* \qquad (7)$$

The net drag coefficient $c_{d,sum}$ is also plotted in fig. 10. The net thrust for the present kinematical flapping case can be determined with

$$c_{thrust} = -c_{d,sum}(\tau = 3) \approx 0.012 \qquad (8)$$

5.1 Comparison of the turbulent shear stress

Equations (4) and (6) describe how to obtain the turbulent shear stress τ_{xy} from numerical and experimental data. The distributions of τ_{xy} shall be compared at four different phase angles:

- 0°: top dead center
- 90°: middle of the downstroke
- 225°: 45° after the bottom dead center
- 270°: middle of the upstroke

The comparison has to be carried out by considering the position of the turbulence wedge[1] and the quantitative value of the turbulent shear stress.

The situation found at the top dead center of motion is depicted in fig. 11. The numerical simulation indicates increased turbulent shear stress in the vicinity of the trailing edge. This corresponds well with the experimental result. However, the experimental magnitude of τ_{xy} is slightly higher and is a consequence of the mixing between the flow of the upper side and the lower side of the airfoil on the trailing edge.

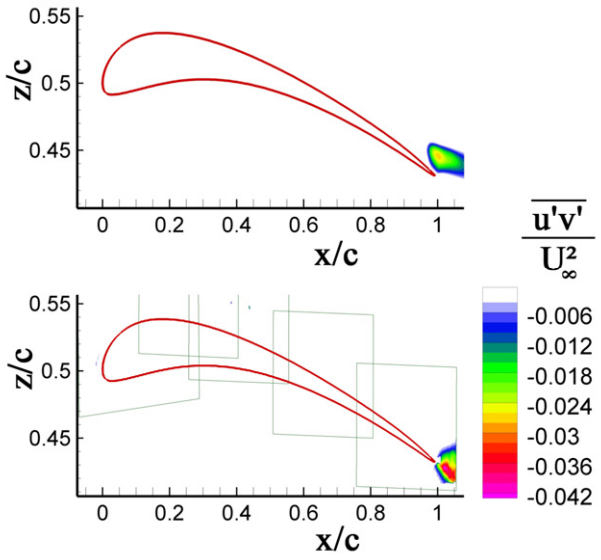

Figure 11: Turbulent shear stress distribution at the top dead center. *Top:* Numerical computation. *Bottom:* Experimental result.

[1] The distribution of the turbulent shear stress indicating turbulent flow forms figuratively a kind of wedge.

In the middle of the downstroke, the transition from laminar to turbulent flow has moved to the leading edge, as drawn in fig. 12. Beyond the apex of the turbulence wedge at 20 percent of chord length, there is a local increase in the thickness of the wedge at 60 percent of chord length. This might be a result of an imbalance in the turbulence model because this behavior was not found in the experiment.

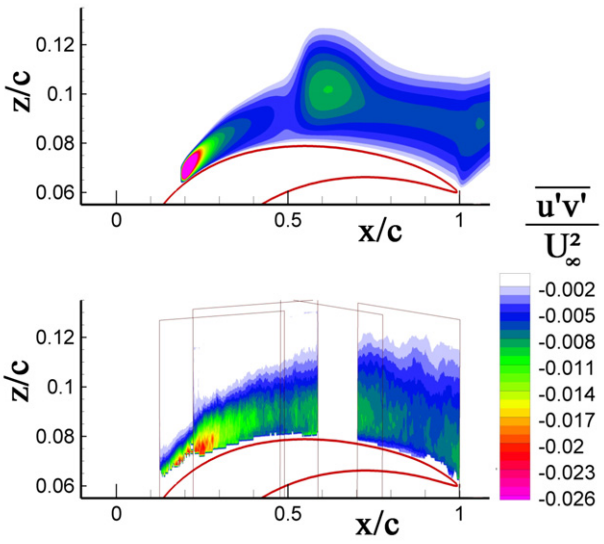

Figure 12: Turbulent shear stress distribution at the middle of the downstroke. *Top:* Numerical computation. *Bottom:* Experimental result.

A quantitative comparison shows good agreement. The peak value of the turbulent shear stress is slightly higher in the numerical prediction; however, due to strong laser light reflections on the airfoil surface, the approximate position of maximum turbulent shear stress could not be captured with experimental data.

At a phase angle of 225°, there is a significant difference between numerical simulation and the measurements, as illustrated in fig. 13. The most likely reason for this discrepancy is maladjustment of the critical N-factor in the numerical simulation. For this purpose, another data collection phase was initiated with the objective to determine the turbulent shear stress distribution of the SG04 airfoil at steady conditions as well. The measurement data can be hopefully used to calibrate the critical N-factor of the numerical model.

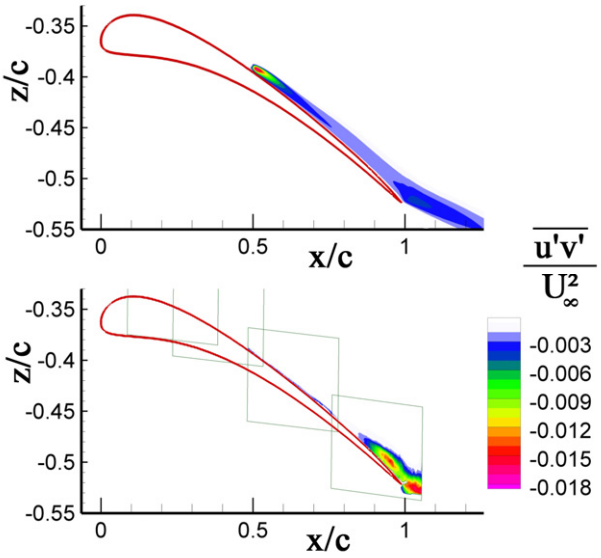

Figure 13: Turbulent shear stress distribution at 45° past the bottom dead center. *Top:* Numerical computation. *Bottom:* Experimental result.

The situation at the middle of the upstroke is depicted in fig. 14. As predicted by the numerical approach, the transition location has moved back to the trailing edge. Also at this phase angle, the transition onset is more upstream in the numerical simulation compared to the PIV dataset. This could be an indicator of a moderate increase in the critical N-factor in the numerical algorithm.

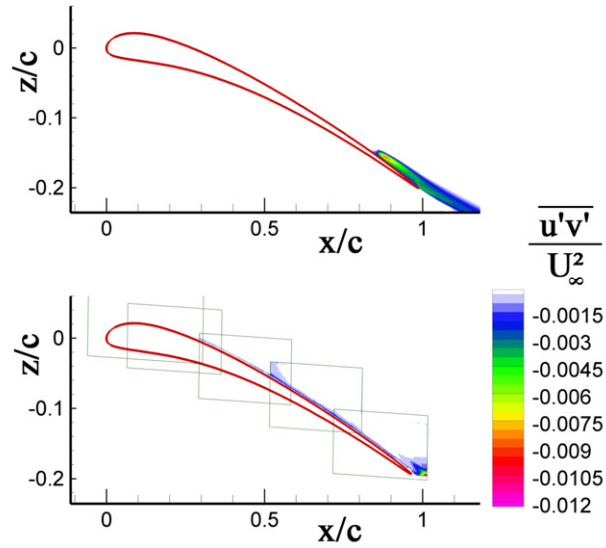

Figure 14: Turbulent shear stress distribution at the middle of the upstroke. *Top:* Numerical computation. *Bottom:* Experimental result.

6 Conclusion

Numerical URANS simulations were performed with the flow solver FLOWer in order to compute the flow around the flapping birdlike airfoil SG04. A validation experiment at the reduced frequency k=0.2 was carried out to verify if the computations are able to predict the real aerodynamic behavior. Therefore, the stereoscopic Particle Image Velocimetry technique was applied to obtain velocity data and turbulent quantities of the boundary layer flow at four different phase angles of the flapping motion. Both numerical and experimental investigations result from much scientific work over the last several years.

By comparing numerical and experimental data, it turned out that the numerical algorithm can predict the movement of the laminar separation bubble – a transition process from laminar to turbulent flow at low Reynolds numbers – during one flapping cycle. This behavior was confirmed with the experimental datasets. However, by comparing the turbulent shear stress distribution of numerical simulation and measurement data, there are still some discrepancies in the transition prediction during the upstroke of the flapping motion. This might be a result of a still maladjusted critical N-factor in the numerical algorithm, which has to be verified in future works.

7 Acknowledgements

This project is funded by the German Research Foundation (DFG) as a part of the priority program SPP 1207. Discussions with Jan Windte on various aspects of the numerical simulations are gratefully acknowledged.

References

[1] Radespiel R, Windte J, Scholz U. *Numerical and Experimental Flow Analysis of Moving Airfoils with Laminar Separation Bubbles*. AIAA Journal, Vol. 45, No. 6, pp 1346-1356.

[2] Unger R, Kleinert J, Haupt M, Horst P, Windte J, Bansmer S, Kähler C, Radespiel R. *Design and Analysis of an Aeroelastic Validation Experiment for*

Moving Flexible Airfoils. CEAS conference, Berlin, Germany, September 2007.

[3] Horton H. *Laminar Separation Bubbles in Two and Three Dimensional Incompressible Flow.* Departement of Aeronautical Engineering, Queen Mary College, University of London, 1968.

[4] Spalart P, Strelets M. *Mechanisms of transition and heat transfer in a separation bubble.* Journal of Fluid Mechanics, Vol. 403, pp 329-349, 2000.

[5] Oertel H, Delfs J. *Strömungsmechanische Instabilitäten.* Springer, Berlin, Heidelberg, 1996.

[6] Bansmer S, Kähler C, Radespiel R, Unger R, Haupt M, Horst P. *A comparison of the flow around a flexible and a non-flexible airfoil for flapping wing propulsion.* 79th Annual Meeting of the International Association of Applied Mathematics and Mechanics, Bremen, April 2008.

[7] Windte J, Scholz U, Radespiel R. *Validation of the RANS-simulation of laminar separation bubbles on airfoils.* Aerospace Science and Technology, Vol. 10, No. 6, pp 484-494, 2006.

[8] Kroll N, Rossow C, Schwamborn D, Becker K, Heller G. *MEGAFLOW: A Numerical Flow Simulation Tool for Transport Aircraft Design.* International Council of the Aeronautical Sciences. Paper No. 1105, Toronto, 2002.

[9] Menter F. *Two-Equation Eddy-Viscosity Transport Turbulence Model for Engineering Applications.* AIAA Journal, Vol. 32, No. 8, pp 1598-1605, 1994.

[10] Schrauf G. *LILO 2.1 User's Guide and Tutorial.* GSSC Technical Report 6, Ver. 2.1, 2006.

[11] Bansmer S, Scholz U, Windte J, Kähler C, Radespiel R. *Flow Field Measurements on an Oscillating Airfoil for Flapping Wing Propulsion.* AIAA 2008-581.

[12] Bansmer S, Kähler C, Radespiel R. *Flow field measurements on a flexible oscillating airfoil for flapping wing propulsion*. 13th International Symposium on Flow Visualization - ISFV 13, NICE - French Riviera , ACROPOLIS Congress Center, 1st - 4th July , 2008

[13] Lang M, Marxen O, Rist U, Wagner S. *Experimental and Numerical Investigations on Transition in a Laminar Separation Bubble.* in: Wagner S, Rist U, Heinemann H, Hilbig R, (eds.) *Notes on Numerical Fluid Mechanics and Multidisciplinary Design*, Vol.77, Vieweg, Braunschweig, 2002, pp 207-214.

[14] Rist U. *Instability and Transition Mechanisms in Laminar Separation Bubbles.* RTO-AVT-VKI Lecture Series 2004, Nov. 24-28, 2003.

[15] Windte J, Radespiel R. *Propulsive Efficiency of a Moving Airfoil at Transitional Low Reynolds Numbers.* AIAA Journal in Print, 2008.

[16] Jones K, Platzer M. *Experimental Investigation of the Aerodynamic Characteristics of Flapping-Wing Micro Air Vehicles.* 41st Aerospace Science Meeting & Exhibit, 6-9 January 2003 / Reno, NV, AIAA-2003-0418.

[17] Jones M, Castro B, Mahmoud O, Pollard S, Platzer M, Neef M, Gonet K, Hummel D. *A collaborative Numerical and Experimental Investigation of Flapping-Wing Propulsion.* 40th Aerospace Sciences Meeting & Exhibit, January 14-17, Reno, NV, USA, 2002.

[18] Anderson J, Streitlien K, Barret D, Triantafyllou M. *Oscillating foils of high propulsive efficiency.* Journal of Fluid Mechanics, Vol 360, 1998, pp. 41-72.

[19] Tuncer I, Platzer M. *Thrust Generation Due to Airfoil Flapping.* AIAA Journal, Vol. 34, 1996, pp. 324-331.

[20] Jones K, Platzer M. *Numerical Computation of Flapping-Wing Propulsion and Power Extraction.* 35th Aerospace Sciences Meeting & Exhibit, January 6-10, Reno, NV, USA, 1997.

[21] Tuncer I, Kaya M. *Optimization of Flapping Airfoils for Maximum Thrust and Propulsive Efficiency.* AIAA Journal, Vol. 43, No. 11, 2005, pp. 2329-2336.

[22] Küssner H. *Zusammenfassender Bericht über den instationären Auftrieb von Flügeln.* Luftfahrtforschung, Vol. 13, 1936, pp. 410-424.

Copyright Statement